Recent advances in grazing-incidence small-angle neutron scattering for interfacial nanostructures in soft matter, magnetic materials, and energy devices

Hai-gang Qin(覃海港)[1,2], Tai-sen Zuo(左太森)[1,2], Chang-li Ma(马长利)[1,2], Chen Zhao(赵晨)[1,2], Hong Zhu(朱宏)[1,2], Hao-tian Cheng(程昊天)[1,2], Shao-yu Lin(林少榆)[1,2], He Cheng(程贺)[1,2†] and Qing Chen(陈青)[1,2†]

[1]*Institute of High Energy Physics, Chinese Academy of Sciences, 10049 Beijing, China*
[2]*Spallation Neutron Source Science Center, 523803 Dongguan, Guangdong, China*

Interfacial phenomena are central to many critical issues in materials science. The nano-to micro-structure at the buried interface serves as a critical determinant of the macroscopic functionality of soft matter, magnetic materials, and energy devices. Conventional X-ray-based techniques suffer from limited sensitivity to light elements (e.g., H, Li) and difficulty in probing the buried interfaces under *operando* conditions. With the substitution of X-ray with neutron, the grazing-incidence small-angle neutron scattering (GISANS) technique overcomes these limitations with its selective penetration depth, higher sensitivity to light elements, and tunability of isotopic contrast. This approach provides critical experimental support for elucidating interfacial structure–property relationships and guiding the rational design of advanced functional materials. In the review, we firstly provide a brief overview of the theoretical framework of the GISANS technique, followed by an examination of the current advancements and instrumentation of GISANS platforms. Then the recent progress of GISANS in understanding interfacial properties in diverse material systems is discussed. Furthermore, we highlight the potential applications of GISANS that extend beyond traditional scientific disciplines.

Keywords: grazing incidence small-angle neutron scattering, neutron scattering instrument, interfacial nanostructure, material science

1. Introduction

In multiphase systems, interfaces serve as transition zones between distinct materials or phases. Typically, these regions are only a few to a few hundred atomic layers thick and exhibit physical and chemical properties that diverge sharply from those of the bulk.[1] Specifically, the deviation arises from confined geometry and non-centrosymmetric environment of interfaces. Such interfacial phases are characterized by broken long-range order, a high density of uncoordinated sites, and reconstructed local electronic densities of states, which underpin a host of functional properties.[2] Interface science is at the heart of modern physical chemistry and acts as

† Corresponding author. E-mail: chenghe@ihep.ac.cn
† Corresponding author. E-mail: chenqing@ihep.ac.cn

a fundamental driver of technological innovation. Historically, significant breakthroughs have depended on the manipulation of interfacial effects. For example, the field-effect transistor is a fundamental component of the semiconductor industry, which functions by modulating band bending and carrier channels at the Si/SiO_2 interface.[3] Similarly, in energy storage, the rate capability and cycle life of lithium-ion batteries depend critically on the kinetics of desolvation, transport, and intercalation at the electrode/electrolyte interface.[4] However, functional interfaces can experience structural relaxation, compositional segregation, or even fracture when subjected to operational stresses like high electric fields, steep concentration gradients, or mechanical strain. These issues can lead to irreversible device degradation. To address these performance challenges, it is essential to thoroughly understand the interfacial microstructure, topology, and composition, as well as their spatiotemporal evolution in situ. This remains a key area of focus in surface and interface science.

The advancement of interface science is closely linked to the development of characterization techniques. By combining multiple techniques, researchers can leverage their respective strengths in resolution, sensitivity, and probing depth to gain a more complete and deeper understanding of interfacial properties and dynamics. Electron microscopy (EM) enables the measurement of sample morphology at the sub-nanometer scale due to the extremely short wavelength of electrons.[5] Atomic force microscopy (AFM) offers atomic-level spatial resolution, which can accurately measure the surface topography and provide intuitive micro-scale topographic maps that help interpret local physicochemical properties.[6] X-ray photoelectron spectroscopy (XPS) can reveal the surface chemistry, including elemental composition, chemical states, and bonding configurations, by analyzing the binding energy. When combined with argon ion sputtering, it also allows for depth detection of elemental distribution beneath the surface.[7]

Neutrons have many advantages when being used as probes. For example, neutrons are electrically neutral and interact directly with atomic nuclei, which result in the strong penetrating power of neutron. The energy of neutrons is typically much lower than that of X-ray photons, which means that neutrons cause almost no radiation damage to samples. Moreover, neutrons are highly sensitive to light elements, such as hydrogen and lithium. They also enable contrast matching by isotopic substitution, which is a powerful technology for measuring the structural features in the area of interest.[8, 9] These advantages make neutrons particularly suitable for studying complex interfaces in soft matter, biomaterials, and energy materials, as well as for performing in situ characterization under realistic working conditions. In addition, because neutrons carry the magnetic moment, they serve as powerful probes for investigating magnetic materials. Neutron reflectometry (NR) can obtain depth-dependent scattering length density and magnetic scattering length density profiles. It has become a well-established tool for studying polymer thin films,[10] magnetic materials,[11] surface coatings,[12] and solid electrolyte interphases in batteries.[13] Moreover, off-specular scattering provides lateral structural information at the micron scale,[14] such as phase separation in polymers[15] and magnetic domain structures.[16]

At grazing incidence condition, the neutron beam strikes the sample at an angle below the critical angle, resulting in total reflection. To maintain the continuity of the wavefunction at the interface, an evanescent wave forms on the other side of the interface, which decays exponentially with depth. Consequently, the neutron scattering occurs only within a thin layer near the surface, whose detection range depends on the penetration depth of the evanescent wave. This is why GISANS is so surface-sensitive. Besides, the probing depth of GISANS can be controlled by tuning the incident angle.[17] However, the grazing-incidence geometry suffers from low neutron flux, leading to long measurement times. Thus, GISANS requires high-brilliance neutron sources to improve the neutron flux. A prime example is the Oak Ridge National Laboratory's facility, which offers a design flux up to 10^{15} n cm^{-2} s^{-1}.[18] This review firstly covers the basic principles and scattering theory of GISANS. Then we highlight recent advances of GISANS's application in materials science. Finally, we discuss future trends and potential applications of GISANS.

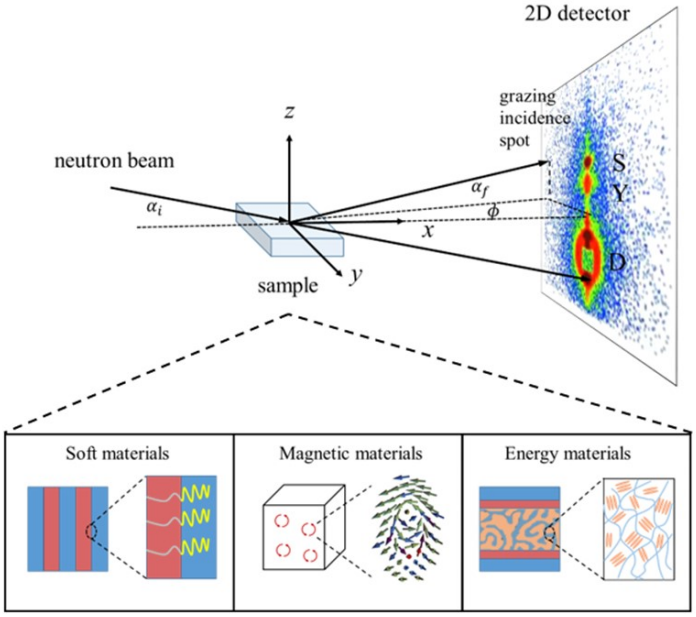


Fig. 1. Schematic illustration of GISANS geometry and its applications in materials science. In the schematic, block copolymers, skyrmions, and organic solar cells serve as representative examples of soft matter, magnetic materials, and energy materials, respectively. S: specular reflection, Y: Yoneda peak, D: direct beam.

2. Basic principles of GISANS

The geometry of the GISANS is shown in Fig. 1, in which the xy plane denotes the sample plane, the projection of the incident beam onto the sample plane is defined as the x axis, and the z axis is perpendicular to the xy plane. The components of the scattering vector Q along the x, y and z directions are given by[19]

$$Q_x = 2\pi(cos\phi \times cos\alpha_f - cos\alpha_i)/\lambda$$
$$Q_y = 2\pi(sin\phi \times cos\alpha_f)/\lambda$$
$$Q_z = 2\pi(sin\alpha_i + sin\alpha_f)/\lambda$$

where λ denotes the wavelength of the neutron, ϕ is the angle between the

scattering direction and the incident plane, α_i and α_f represent the incident angle and scattering angle, respectively. After interacting with the sample, the scattered neutron is detected by a 2D detector. Specular scattering is obtained when the exit angle equals the incident angle, which yields the depth-resolved scattering length density (SLD) profiles. When the exit angle differs from incident angle, the scattering remained within the incident plane is called as off-specular scattering. Scattering outside the incident plane forms the GISANS signal.

In contrast to transmission-mode small-angle neutron scattering (SANS), GISANS operates using a reflection geometry. This approach employs total reflection to minimize the bulk signal. The evanescent wave is formed when the neutron undergoes total reflection at the interface, which propagates along the interface and decays exponentially normal to the surface, allowing us to probe surface and interfacial structures. During GISANS experiments, the incident angle is adjusted to be below the critical angle. The critical angle for total reflection is given by[20]

$$\alpha_c = \lambda \sqrt{\frac{Nb}{\pi}}$$

where Nb denotes the scattering length density. The scattering length density (SLD) does not change linearly with the atomic number of elements, nor with changes in isotopes. In particular, the scattering lengths of hydrogen (H) and deuterium (D) have opposite signs. In polymer and biological research, this feature is used to generate contrast, so that researchers can selectively study specific parts of a sample's structure.

GISANS is described by the distorted wave Born approximation (DWBA), which is a first-order perturbation theory.[21] For thick films, the differential scattering cross-section can be approximated as[22]

$$\frac{d\sigma}{d\Omega} = A(Nb)^2 |T_i|^2 |T_f|^2 F(q)$$

in which A denotes the neutron irradiation area, T_i and T_f represent the Fresnel transmission coefficients, and the diffuse scattering factor $F(q)$ can be expressed as

$$F(q) \approx NP(Q)S(Q)$$

where $P(Q)$ is the form factor of a single object, and $S(Q)$ is the structure factor that describes the spatial distribution of these objects. Specifically, the form factor mainly depends on the geometry and SLD difference of individual scattering object. Different shapes, such as spheres, cylinders, cubes, and core-shell structures, have their own analytical expressions for $P(Q)$. The structure factor accounts for the interference between scattering waves from different particles, which is determined by the spatial correlation and interactions among particles. In the dilute limit, $S(Q)$ approaches unity.[23] However, it is quite difficult to fully fit 2D GISANS scattering patterns with theoretical models. One reason is instrumental smearing, in which the finite wavelength spread, beam divergence, and large beam footprint blur the measured pattern. This effect has recently been quantified within a forward-synthesis framework for hard-sphere colloids, in which spectra with and without smearing are generated systematically.[24] Therefore, researchers usually take a qualitative approach

for data analysis. For example, slicing the scattering pattern along different directions can index liquid crystal phases,[25] measure repeat spacing, and extract form factors.[26] Specialized software packages, such as IsGISAXS,[27], fitGISAXS,[28] and BornAgain[29] are widely used, which have greatly advanced the detailed analysis of GISANS data. These tools are based on DWBA, which means that these softwares can accurately handle optical effects in grazing-incidence geometry, including refraction, total reflection, and multiple scattering. This capability facilitates the connection of measured 2D scattering patterns to real structural models. However, this kind of modeling is time-consuming and requires significant expertise. As scattering data volumes grow rapidly, there is an increasing demand for fast, model-free processing. One such tool is ScatterX,[30] which performs batch reduction, background correction, and visualization of high-throughput scattering data through matrix operations.

3. GISANS instruments and sample environments

To date, a GISANS-specific instrument has not been developed. Instead, GISANS is generally conducted on small-angle neutron scattering (SANS) instruments or neutron reflectometers.[17] GISANS requires precise sample alignment: on the one hand, to ensure that the neutron beam strikes the sample at a grazing incidence angle; on the other hand, precise control of the angles α_i and ψ is a necessary condition for the alignment and measurement of thin-film samples. Angular distortions will lead to distortions in the Q_y-Q_z mapping, which leads to GISANS degenerating into conventional diffuse or off-specular scattering.[31] In SANS instruments, GISANS is typically accomplished by incorporating a sample tilting stage, which transforms the original transmission geometry into a grazing-incidence geometry.[32] For reflectometers, a two-circle goniometer is employed to accurately regulate both the incident angle and the tilt angle relative to the scattering plane.[33] In light of the low neutron flux and the considerable time needed for direct alignment with the neutron beam, it is advised in the literature to initially align the sample using a laser before proceeding to neutron beam measurements.[31] To improve the Q_y resolution for probing the in-plane structure of the sample, the slab-shaped beam used in conventional diffuse or reflectivity experiments should be replaced with a point-shaped beam.[32] Additionally, due to the limited brilliance of neutron sources, GISANS counting times are often on the order of hours. It has been reported that the neutron flux can be significantly increased by changing the sample installation from vertical to horizontal on a reflectometer[34] or by installing mirror optical assemblies on SANS beamlines to alter the neutron beam shape.[35] So far, the reported GISANS instruments, along with their parameters and implementation methods are summarized in Table 1.

Table 1. GISANS parameters and their implementation at current neutron sources

Instrument/ Neutron source	Q range ($\mathrm{Å^{-1}}$)	Neutron flux (n cm^{-2} s^{-1})	Implementation
VSANS/CSNS[36]	Q_y:1×10^{-4}~0.05	1×10^{7}	Combining two four-blade

	Q_z:0.001~0.05		slits and a multi-slit array to achieve the GISANS and GI-VSANS geometries
SANS/CSNS[37]	$Q_{y,z,max}$:0.05	/	/
SANS-suanni/CMRR[32]	$Q_{y,z}$:0.005~0.3	4×10^6	Front and back four-blade slits
Maria/MLZ[38]	Q_y:0.002~0.15 Q_z:0.002~2.1	2×10^7	Pinhole collimation via two four-segment slits and an absorber blocking vertical focusing
KWS-1/MLZ[39]	$Q_{y,z}$:7×10^{-4}~0.5	~1×10^8	Custom-designed sample-position hexapod with rectangular slit collimation
KWS-2/MLZ[40]	$Q_{y,z,max}$:0.1	/	Rectangular slit collimation with sample tilting/rotation
Bio-SANS/ORNL[41]	$Q_{y,z}$:0.003~0.067	~1×10^7	/
EQ-SANS/ORNL[42]	$Q_{y,z}$:0.002~1.4	~1×10^7	Sample goniometer and slit beam shaping
REFSANS/FRM II[43]	Q_y:10^{-7}~0.3 Q_z:9.5×10^{-4}~0.8	~1×10^4	Switchable collimation: radial collimator generates up to 13 sub-beams point-focused at the 2D detector for GISANS; NR/GISANS auto-switch within minutes; single incident angle ToF yields full penetration curve
D22/ILL[25]	$Q_{y,z,max}$:0.02	/	Point-beam collimation with vertical sample geometry
D33/ILL[44]	$Q_{y,max}$:0.02 $Q_{z,max}$:0.02	/	Sample goniometer and slit collimation
Super ADAM/ILL[34]	$Q_{y,max}$:0.02	/	Π-GISANS: horizontal sample geometry on reflectometer Super ADAM; fan-shaped beam with vertical divergence from HOPG monochromator
SANS2D/ISIS[45]	$Q_{y,max}$:~0.1 $Q_{z,max}$:0.1	/	Transmission ToF-SANS converted to GISANS via slit beam shaping at grazing incidence; depth-resolved through wavelength-band integration of the ToF spectrum

HEKATE/ESS[46]	$Q_{y,min}$:~1×10^{-4} Q_z:10^{-3}~0.3	2×10^{10}	Two Selene neutron guides with spatially separated wavelength frames; low-background design
SAGA/ESS[47]	/	/	ToF mode
HBS[48]	Q_y:0.002~1.8 $Q_{z,max}$:0.2	2.2×10^{6}	ToF-SANS converted to GISANS: single direct beam on horizontal sample with reduced vertical divergence; dual detectors
Quokka/ANSTO[49]	/	/	/
SHARAKU/J-PARC[50]	/	/	TOF-GISANS uses an elliptically shaped NiC/Ti focusing supermirror for point-to-point beam focusing, combined with time-of-flight wavelength resolution.

The understanding of the relationship between stimuli and material responses is essential for effectively controlling the performance of the final product or device. For example, a composite material made of poly(3,4-ethylenedioxythiophene):poly(styrene sulfonate) (PEDOT:PSS) and sodium carboxymethyl cellulose (NaCMC) can be synthesized by physical crosslinking and hydrogen bonding, which exhibits humidity-responsive actuation. Moreover, the composite shows excellent structural, mechanical and electrical self-healing properties when subjected to alternating dry and humid gas conditions, making it an excellent choice for applications in smart soft robotics.[51] Researchers are interested in monitoring the alteration of material properties in response to external stimuli, including temperature, humidity, pressure, and magnetic fields, during GISANS investigations. The sample environment can apply these stimuli to sample, facilitating the study of changes under external fields or chemical conditions during GISANS measurements. The sample environments applicable to GISANS experiments are listed in Table 2.

Table 2. sample environments of GISANS

External fields	Instrument/ Neutron source	Parameter range
Temperature	ESS	10~80°C[33]
	D22/ILL	25~45°C[52]
	SANS2D/ISIS	20~100°C[53]
	FIGARO/ILL	4~20°C[54]
	D22/ILL	30~70°C[55]

Humidity	ESS	0~96%RH[33]
	ILL	40~100%RH[56]
	SANS2D/ISIS	25~90%RH[53]
Langmuir trough	KWS-2/MLZ	68 × 5 mm[57]
	Super ADAM/ILL	60 × 80 mm[34]
Pressure	D22/ILL	0.1~100 MPa[58]
	D22/ILL	1~80 bar[52, 59]
Magnetic field	KWS-2/MLZ	0.4 T[60]
	D33/ILL	1.5 T[61]
	SHARAKU/J-PARC	7 T[62]
	Quokka/ANSTO	7 T[63]
Sheer rate	ADAM/ILL	2500 s^{-1}[64]
	FIGARO/ILL	0.1~1000 s^{-1}[65]
Electrical current/voltage	REFSANS/MLZ	-11~11 V, -0.6~0.6 A[66]

4. Applications of GISANS in material science

4.1. Soft matter

Soft matter encompasses a diverse range of complex condensed materials that occupy the space between simple liquids and ideal solids. This category includes entities such as polymers, colloids, surfactants, liquid crystals, and bio-macromolecules. The fundamental units of soft matter, including molecules and colloidal particles, often undergo self-assembly into ordered or functional meso/macroscopic structures through non-covalent interactions. For example, surfactants form self-assembled structures such as spheres and rods. These ordered structures are highly sensitive to external stimuli, including temperature, mechanical stress, electric fields, magnetic fields, and humidity. Even tiny perturbations can trigger drastic changes in their structure and properties, which gives soft matter stimuli-responsive characteristics, making it suitable for fabricating various smart responsive devices.

4.1.1. Self-Assembly of Block Copolymers

The block copolymer is the polymer which consists of two or more chemically distinct polymer blocks. When immiscible blocks are linked by covalent bonds, they undergo thermodynamically driven microphase separation and self-assembly. Consequently, the block copolymers yield ordered nanostructures, including lamellae, cylinders, and spheres.[67] Moreover, the microphase behavior of block polymers can be tuned by adjusting block length, composition ratio, and the Flory-Huggins

interaction parameter χ.[68, 69] Block copolymers exhibit controllable microphase separation and diverse self-assembled morphologies, making them useful in many fields. For example, adjusting molecular structures results in separation membranes with customizable pore sizes for different separation scenarios.[70] GISAXS benefits from the wide availability of synchrotron sources, high photon flux, and short measurement times, so it is widely adopted in block copolymer research. Nonetheless, GISAXS encounters difficulties in differentiating block copolymers with analogous chemical structures and exhibits limited sensitivity to buried interfaces composed of light elements. In contrast, GISANS provides distinct advantages in the characterization of light elements by utilizing neutrons as the probe, which facilitates the clear resolution of block copolymer microphase structures and buried interfaces containing light elements. Additionally, deuteration enables researchers to effectively distinguish between different domains within block copolymers.[71]

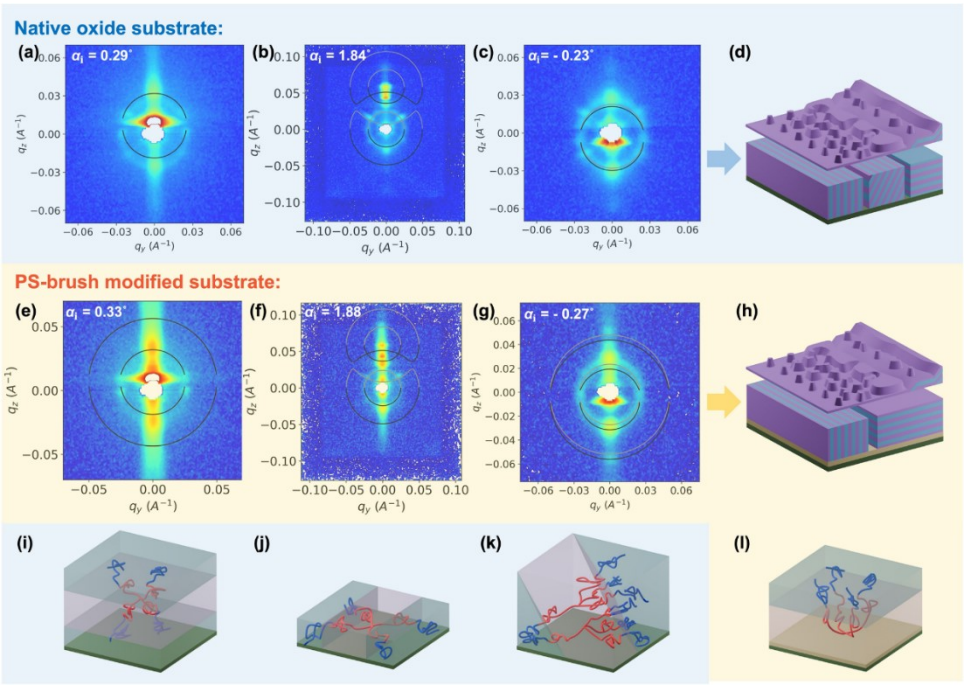


Fig. 2. Effect of substrate types on the self-assembly structure of 4-arm star block copolymer. (a-c) GISANS images on native oxide substrate (e-g) GISANS images on PS-brush modified substrate. (d, h) Diagrams of self-assembly of 4-arm star block copolymer on two types of substrates. (i-k) Chains conformation on native oxide substrate. (l) Chains conformation on PS-brush modified substrate. Reprinted with permission from Ref.72. Copyright 2025 American Chemical Society.

Triblock copolymers are capable of forming micelles in aqueous environments. When these micelles deposit on silicon substrates, they can accumulate into relatively thick films comprising 100–1000 micelle layers. The structural characteristics of these films are influenced by the surface groups present on the substrate. [72] Hu et al.[73] studied the depth-dependent orientation of block copolymer self-assembly using GISANS. They synthesized polysulfone methacrylate-block-polystyrene copolymers through hydrolysis, observing that the microphase-separated structures exhibited distinct orientations at the polymer/air and polymer/substrate interfaces.

Surface-induced parallel lamellae were effectively extended from the interface into the bulk material. Conversely, the vertical orientation was restricted to the region near the interface and did not propagate through the film thickness. This observation indicates that interfacial energy plays a crucial role in governing the parallel alignment. Gan et al.[74] achieved precise control over thin-film morphology by modifying the substrate. They synthesized multi-arm star copolymers with a polystyrene (PS) core and poly(2-vinylpyridine) (P2VP) coronas, which exhibited lamellar microdomains. Using the GISANS measurements, they studied the effect of substrate types on the phase-separated structures of a 4-arm star block copolymer (Fig. 2). Substituting the native silicon substrate with a PS-brush layer alters the orientation of the 4-arm star block copolymer film. Initially, the film exhibits a depth-dependent mixed orientation, with parallel lamellae at the interfaces and tilted or random lamellae extending into the bulk. However, the introduction of the PS-brush layer results in a uniform, depth-independent parallel morphology. This transformation is driven by selective interactions between the PS core and the brush, which permit the P2VP corona to reorient upwards, thereby optimizing enthalpic contacts. This study illustrates that the choice of substrate significantly affects the morphology of thin films.

Defects that emerge during the microphase separation of block copolymers have a profound impact on their engineering applications. In semiconductor device patterning, the removal of dislocations and grain boundaries is crucial to achieving high yield and fidelity in pattern transfer.[77] Conversely, in applications such as separation membranes and ion transport systems, the presence of controlled defects can enhance permeation flux and facilitate efficient particle transport pathways.[78, 79] At spallation neutron sources, neutrons with a range of wavelengths were utilized in time-of-flight GISANS (TOF-GISANS). This technique enables the concurrent examination of both surface and bulk structures, providing a non-destructive and statistically significant analysis of defect structures.[80] Müller-Buschbaum et al.[81] examined the morphology of deuterated polystyrene-block-poly(methyl methacrylate) copolymer films, which were characterized by numerous defects, using TOF-GISANS. The analysis reveals a lamellar microphase-separated structure with numerous defects. As a consequence, the film is composed of small, randomly oriented grains, each averaging 300 nm in size. Within these grains, there are 4 to 5 repeating lamellae, with a spacing of 67 nm between them.

Taken together, these studies define the specific role of GISANS in block copolymer thin films. GISAXS is excellent for detecting the lattice of microdomain in block copolymer. While it cannot attribute the scattering to a particular block, owing to the chemically similar in block polymer. Neutron reflectivity yields a one-dimensional depth profile that is averaged over the film plane, so it reveals how composition varies with depth but carries no information on in-plane grain structure. Selective deuteration gives neutrons the contrast needed to distinguish the two blocks. In TOF-GISANS, the probing depth can be changed by altering the wavelength of neutron. Therefore, a single fixed incident angle already samples the film at several depths. Together, these turn one measurement into a depth-resolved map of block

identity and in-plane orientation. Despite these advances, several questions remain beyond the reach of GISANS. The low flux of neutron in GISANS leads to long exposure times, which hinders the detection of time-resolved studies of ordering kinetics in block copolymers. Besides, the deuteration is necessary to increase the contrast, while it also changes the properties of block copolymers by isotope effect.

4.1.2. Polymer Brushes

Polymer brushes are composed of polymer chains, each of which is covalently bonded at one end to a solid substrate. When the grafting density is elevated, steric repulsion arises among adjacent chains. This repulsion compels the chains to extend perpendicularly from the surface, resulting in a distinctive brush-like configuration. [82] The surface characteristics of polymer brushes can be modified through deliberate molecular design, optimized fabrication techniques, and the application of external stimuli.[83] Owing to the diverse surface architectures, excellent tunability, and rapid stimuli responsiveness, the polymer brushes are widely applied in smart responsive films,[84] anti-biofouling surfaces,[85] and functional surface coatings.[86] GISANS offers a non-destructive method for the comprehensive characterization of lateral nanostructures and phase separation behaviors in polymer brushes. By incorporating specialized sample environments, such as high-pressure and variable-temperature modules, GISANS is capable of monitoring stimulus-induced structural evolution at the brush-substrate interface. This technique provides crucial structural insights into the mechanisms of interfacial phase separation in polymer brushes, facilitating the establishment of quantitative relationships between structure and properties, which is essential for their informed design in practical applications.

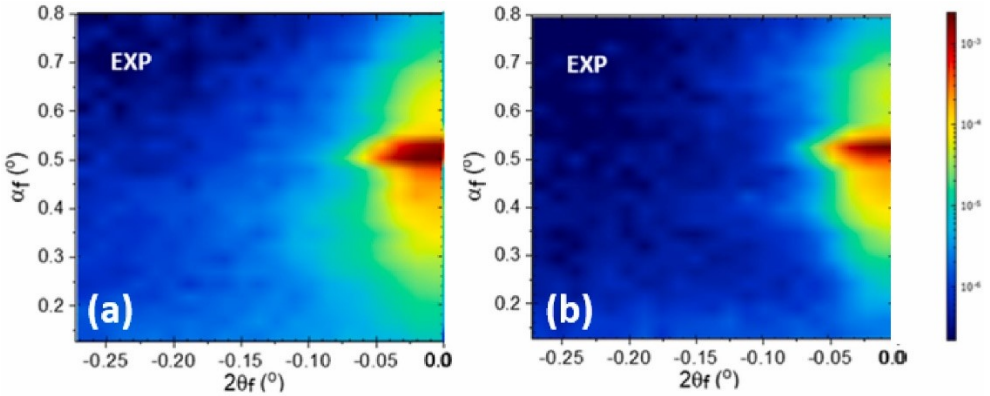


Fig. 3. GISANS data for POFPMA/PDMAEMA mixed brush at different pressure, (a) P = 1 bar and T = 45°C, (b) P = 800 bar and T = 45°C.[52] Reprinted from Fig. 8 of Ref. 52, Copyright 2024, with permission from Elsevier.

Mixed polymer brushes are made of two or more types of polymers with different chemical properties, which attach to the same surface. Typically, the various components exhibit enthalpic incompatibility, leading to microphase separation and the formation of nanoscale domains under confinement conditions. The composition and structure of the outermost brush layer can be dynamically adjusted by external factors such as solvent, temperature, and pH. This allows for the reversible alteration of surface properties, making it suitable for smart applications.[87] In 2024, Vagias et al.[59] reported the first high-pressure grazing-incidence small-angle neutron scattering

(HP-GISANS) characterization of soft matter films at solid-liquid interfaces, enabling in situ probing of in-plane nanostructures under high-pressure conditions. In their subsequent studies, they used mixed polymer brushes, specifically poly(2,2,3,3,4,4,5,5-octafluoropentyl methacrylate) (POFPMA) and poly(2-(dimethylamino)ethyl methacrylate) (PDMAEMA) as model systems to examine how inter-polymer incompatibility affects interfacial nanostructures. These investigations were conducted under swollen conditions in D_2O to observe the resulting changes in structure.[52] By utilizing a mixed brush composed of the highly incompatible hydrophobic POFPMA and the hydrophilic PDMAEMA as a model system, they observed that elevating the pressure from 1 bar to 800 bar led to notable nanostructural changes within the brush layer (Fig. 3). Hydrophobic cylindrical microdomains were identified in the subsurface area through GISANS measurements. Simulations of off-specular reflectivity showed that the hydrophilic aggregates rich in PDMAEMA had a significant surface coverage, with interdomain spacing surpassing 100 nm. Notably, temperature and pressure were found to exert antagonistic effects in tuning the interfacial architecture of the polymer brushes. Here GISANS answers a question that GISAXS and NR cannot answer. It reveals the in-plane structure of a brush at a buried solid–liquid interface under hydrostatic pressure. However, the solvent must be contrast-matched to suppress the bulk signal, so only a narrow range of D_2O/H_2O ratios can be used. Counting times of hours also limit the pressure and temperature range of a single experiment.

4.1.3. Surfactants

The performance of surfactants on a larger scale is influenced by their internal structure. When the concentration of surfactants goes beyond the critical micelle concentration (CMC), the resulting changes in micelle dimensions and their morphological transformations greatly boost the ability to dissolve nonpolar substances.[88] At the solid-liquid interface, surfactants form adsorbed structures, where temperature exerts a pronounced influence on the architecture of the interfacial layer. Steitz et al.[89] employed GISANS to investigate the temperature-dependent behavior at the interface between silicon and D_2O solutions of the nonionic surfactant C_8E_4. Their findings indicated that the surface coverage of C_8E_4 on silicon is significantly temperature-dependent. Specifically, an increase in temperature alone can cause a transition from a state of non-adsorption to one where the surface is entirely covered. Microemulsions, which arise from the combination of surfactant, water, and oil in ternary systems, play a crucial role in various applications such as drug delivery, functional food formulations, and enhanced oil recovery. Their significance is attributed to their exceptionally low interfacial tension and stable thermodynamic properties. Moreover, the effectiveness of these systems is heavily influenced by their interactions with solid interfaces. Vargas-Ruiz et al.[75] utilized a combination of SANS, NR, and GISANS to explore the bulk and interfacial structures of microemulsions that are stabilized by sugar-based surfactants. SANS measurements revealed that microemulsions formulated with tetradecane as the oil phase exhibited smaller domain sizes and a larger renormalized bending modulus

compared to those using methyl oleate. Furthermore, by integrating NR and GISANS, the authors probed the structural evolution of microemulsions upon contact with interfaces of varying polarity. NR profiles indicated a transition from a bulk bicontinuous morphology to a lamellar structure proximal to the substrate. Concomitantly, GISANS data showed no additional in-plane ordering signals beyond those arising from the propagation of the bulk bicontinuous structure, confirming that the lamellar arrangement is confined to an ultrathin region adjacent to the substrate.

4.1.4. Biological Membranes

Biological membranes act as barriers that selectively allow substances to pass, surrounding both cells and organelles. Their main structural component is a bilayer of phospholipids, which is interwoven with macromolecules like proteins and carbohydrates. Structural abnormalities in these membranes are implicated in various pathologies, while a thorough understanding of their architecture is crucial for rational drug design.[90] GISANS provides significant advantages for the analysis of biological membrane structures. It allows for the non-invasive examination of lipid bilayer microstructures and supports real-time observation of membrane reactions to external factors in their natural hydrated state. Furthermore, by adjusting the H_2O/D_2O ratio, it enables the differentiation of specific components, such as lipid tails, headgroups, or protein segments.[91] Paracini et al.[76] developed large-area silica nanoparticle arrays to serve as substrates for examining the structure of lipid bilayers supported by nanoparticles. Neutron reflectometry (NR) confirmed that a highly covered lipid bilayer was established on both the spherical particles and the underlying silica substrate. Complementary GISANS measurements revealed an 84 Å increase in the apparent nanoparticle diameter upon incorporation of hPOPC, which is consistent with the NR results. Contrast matching in water is the decisive advantage for membranes when compared with other non-neutron characterization techniques. The head groups and protein moieties of membrane can be highlighted or nulled by varying the H_2O/D_2O ratio the tails, which is impossible in electron microscopy. However, it takes hours to acquire a full GISANS pattern, while the structural change of interest takes seconds. As a result, GISANS cannot be used to investigate the kinetics of membrane at present, owing to the low neutron flux.

4.2. Magnetic Materials

In power electronic components, magnetic materials are essential for converting, transmitting, processing, and storing both information and energy. Consequently, these materials are extensively used in motors, home appliances, automatic control systems, and information technology. Generally, the performance of magnetic materials is governed not only by composition, but also critically by microstructural characteristics such as magnetic domain texture, correlation length, and magnetic correlations.[92] GISANS exploits the interaction of neutrons with both atomic nuclei and magnetic moments, allowing it to perform two distinct roles. On one hand, nuclear scattering profiles elucidate nanoscale lateral structures, interfacial topography, and periodicities within thin films and multilayers. On the other hand,

under polarized neutron conditions, magnetic scattering allows for the investigation of domain texture, magnetic correlations, and depth-resolved magnetization profiles. This endows GISANS with the unique capability to provide simultaneous structural and magnetic insights into magnetic materials at the nanoscale.[60]

4.2.1. Skyrmions

Skyrmions are a unique form of chiral magnetic structures, distinguished by their vortex-like spin patterns on a nanoscale. Their remarkable stability, which is due to the conservation of topological charge, makes them highly suitable as potential information carriers in the development of advanced magnetic memory and logic devices. Within thin films or multilayers, these entities often organize themselves into lattice structures with lateral periodicity.[93] Since neutrons carry a magnetic moment, neutron characterization techniques are ideally suited for probing skyrmions. Among them, polarized off-specular neutron scattering under conditions facilitates depth-resolved investigations of structural and magnetic correlations at the micrometer scale. In contrast, polarized GISANS extends this capability to the nanometer scale, making it an essential tool for examining skyrmions, which typically measure between 20 and 300 nm.[94] Liyanage et al.[95] investigated three-dimensional skyrmions in Fe/Gd multilayers by combining of PNR, SANS, and GISANS. PNR and SANS were used to examine magnetic structures both in-plane and averaged over depth. At the same time, GISANS allowed for the observation of structural details in both in-plane and out-of-plane directions. The GISANS results were found to be consistent with physical micromagnetic models. This agreement guides the design of heterostructures with artificial soft magnetic layers, which enhance the stability of skyrmion. In a related study, Wiedemann et al.[96] investigated the magnetic ordering in thick epitaxial MnSi films grown on Si(111) substrates by using GISANS and off-specular reflectivity (OSR). The resulting magnetic phase diagram closely matches that of thick epitaxial FeGe films, indicating that the observed magnetic order is universal. This work provides a valuable starting point for interpreting how established deposition techniques can be leveraged to tailor skyrmion properties in nanoscale systems. For an exposed skyrmion lattice, resonant magnetic GISAXS gives equivalent reciprocal-space information in seconds. GISANS is then unnecessary. GISANS is preferred when nuclear and magnetic contributions must be separated in one dataset. In some cases, it is the only option.

4.2.2. Patterned Artificial Spin Systems

Artificial spin systems are assembled from nanoscale single-domain ferromagnets arranged on periodic or aperiodic lattices. Owing to the constraints imposed by the lattice geometry, the dipolar interactions among all nanomagnets cannot be simultaneously satisfied, a phenomenon known as geometric frustration. This frustration gives rise to a vast manifold of nearly degenerate states and a rich variety of metastable micro configurations. Consequently, artificial spin systems serve not only as versatile platforms for probing fundamental physics, but also as promising candidates for multi-bit information storage.[97] Given that these systems comprise a large ensemble of nanomagnets, GISANS is particularly well-suited for characterizing

them. It provides statistically significant correlation information over macroscopic areas in reciprocal space, resolves short-range spin correlation lengths via diffuse scattering, and identifies long-range ordered structures through Bragg peaks.[98] Pip et al.[99] investigated the spin correlation behavior in artificial triangular lattice Ising spin systems using GISANS (Fig. 4). They developed an empirical magnetic structure factor and incorporated it into the DWBA formalism. Fitting the GISANS data revealed that both symmetric and compressed lattices exhibit extremely weak correlations reminiscent of paramagnetism. Notably, the compressed lattice favors the formation of stripe-like correlations oriented along the direction of distortion. The main advantage of GISANS here is statistics. Magnetic force microscopy and photoemission electron microscopy show the state of a single nanomagnet, but their field of view is only tens of micrometres. GISANS averages over about macroscopic area at once. It therefore gives correlation lengths with a known uncertainty, which the imaging methods cannot provide.

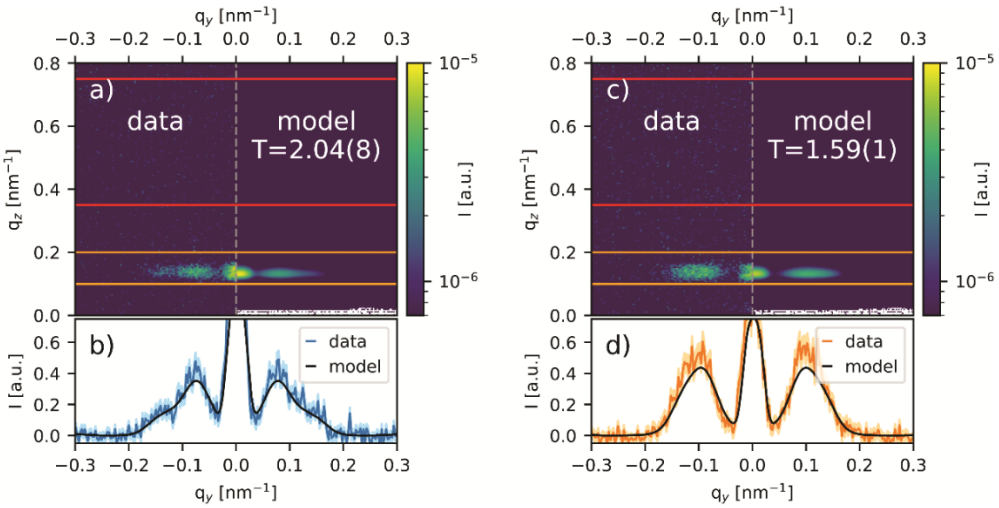


Fig. 4. GISANS data of an artificial Ising spin ice. (a, c) GISANS scattering intensity maps at different effective temperatures; (b, d) corresponding integrated intensity curves compared with fits to respective models for (a) and (c).[99] Reproduced from Fig. 5 of Ref. 99 with permission from The Royal Society of Chemistry. Copyright 2021, Royal Society of Chemistry.

4.3. Energy Devices

The combustion of fossil fuels is fundamental to industrial development. However, it results in the release of substantial quantities of CO_2, thereby increasing atmospheric concentrations. As a result, the increasing CO_2 level in atmosphere leads to various global challenges such as climate warming and extreme weather events. To mitigate the carbon emissions issue, energy devices have seen rapid growth in recent years, which were utilized to store the renewable energy, such as wind and solar.[100] The performance of these devices is typically governed by interfacial properties. For instance, photocurrent generation occurs at the donor-acceptor interface in organic solar cells.[101] In lithium-ion batteries, the passivation layer at the electrode-electrolyte interface plays a pivotal role to the cycle life of batteries.[102]

Similarly, the triple-phase boundaries (TPBs) formed among the electrolyte, catalyst, and reactant gases is considered to determine the power output in fuel cells.[103] GISANS offers distinct advantages for characterizing such interfaces. It probes variations in morphology, pore structure, and porosity, making it particularly well-suited for energy devices with complex compositions and buried interfaces.

4.3.1. Organic Solar Cells

The performance of organic solar cells (OSCs) is largely dictated by the morphology, phase separation, and molecular mixing within the photoactive layer. To ensure efficient exciton dissociation and charge transport, a nanoscale bicontinuous interpenetrating network formed by the donor and acceptor materials is generally desired.[104] GISANS is capable of resolving the fine structural details of the active layer, providing critical insights for establishing structure–property relationships. Lu et al.[37] demonstrated the amorphous Y6 aggregates within the PM6:d-Y6 photoactive layer by using GISANS measurement. Larger amorphous acceptor was found to be helpful to improve the performance of OSCs, which facilitated interconnected charge-transfer pathways, enhanced charge extraction, and suppressed non-radiative recombination. In subsequent work, the same team incorporated a significant amount of the small-molecule acceptor BTR-Cl into PM6/Y6 blend films.[105] The strategy resulted in surpassing the traditional thickness limitation of active layers, which is typically less than 100 nm for achieving high efficiency. As a result, a remarkable power conversion efficiency of 17.7% was achieved at an active layer thickness of 300 nm. Moreover, the aggregation of Y6 molecules was promoted within the ternary blend by incorporating BTR-Cl, which was characterized by selective deuteration and TOF-GISANS measurements. (Fig. 5). It also enhanced the interconnectivity between the donor and acceptor phases, ultimately pushing the upper limit of the active layer thickness. The advantage of GISANS here lies in attribution rather than in morphology. Resonant soft X-ray scattering cannot assign the structure to a specific component without assumptions about the optical constants.

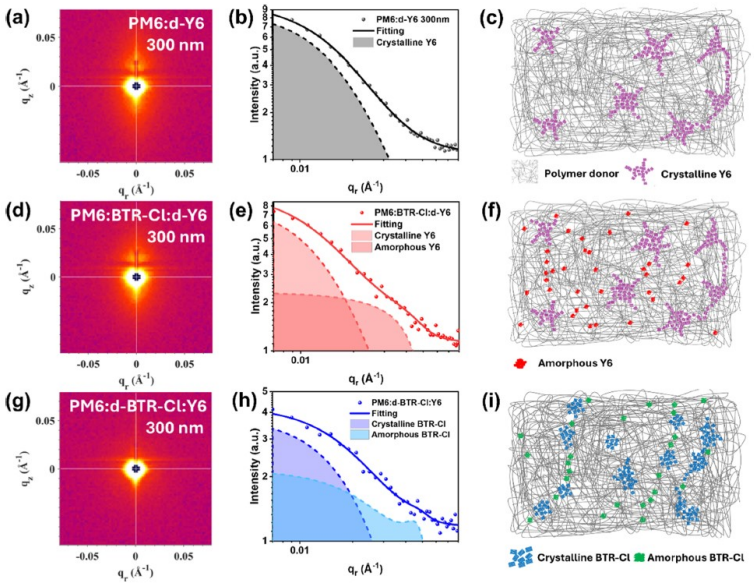


Fig. 5. TOF-GISANS results of a 300 nm-thick blend film. (a, d, g) TOF-GISANS patterns of PM6/d-Y6, PM6/BTR-Cl/d-Y6, and PM6/d-BTR-Cl/Y6. (b, e, h) Horizontal cuts (points) and best-fit curves (lines) corresponding to (a), (d), and (g). (c, f, i) Schematic illustrations of the blend film structures proposed by the authors based on the GISANS fitting results.[105]

4.3.2. Lithium ion batteries

The performance of lithium-ion batteries is influenced by several factors, notably the characteristics of electrode materials. These include the type of active material, particle size, porosity, electrode thickness, and the distribution of the conductive network. Additionally, the physicochemical properties of the solid electrolyte interphase (SEI) are particularly critical.[106] Gilles et al.[107] investigated the structural parameters of TiO_2 nanotube array anodes before and after Si coating by using TOF-GISANS (Fig. 6). TOF-GISANS enabled the determination of both the pore size and spacing of TiO_2 nanotubes, while also revealing the internal pore structure of the electrode. This structural information is typically beyond the reach of SEM characterization. Integrating the structural insights from GISANS with theoretical calculations is expected to elucidate the structure–property relationships, which facilitates the development of high-performance batteries. However, to the best of our knowledge, GISANS has not yet been applied to characterize the solid electrolyte interphase, which remains one of the key interfacial challenges in lithium-ion batteries. Closing this gap requires contrast matching with a deuterated electrolyte, an electrochemical cell geometry compatible with grazing incidence, and high neutron flux.

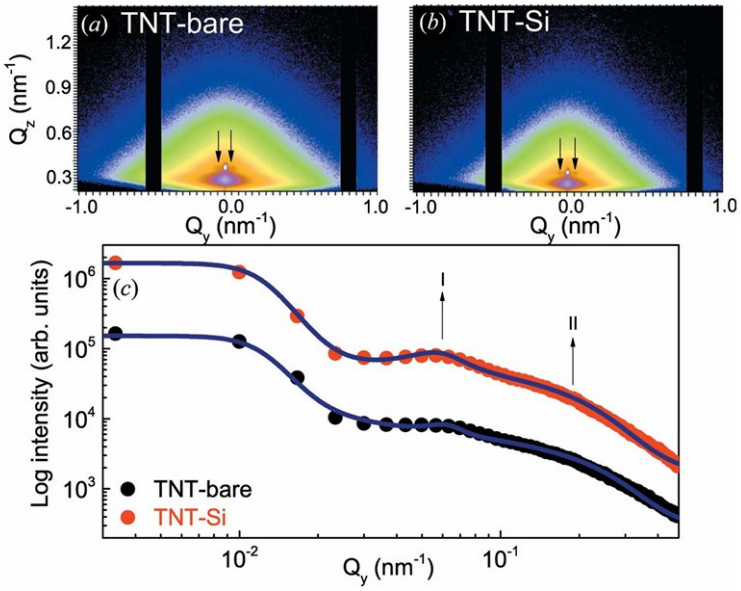


Fig. 6. GISANS data of anode for lithium ion batteries. (a) TiO_{2-x}-C nanotubes (TNT bare), (b) Si/TiO_{2-x}-C nanotubes (TNT-Si), (c) integrated intensity curve from a horizontal slice at $Q_y = 0.37$ nm^{-1} and the corresponding fit curve.[107]

4.3.3. Fuel cell

The membrane electrode assembly (MEA) is the core of a fuel cell, which typically consists of hot-pressed anode and cathode catalyst layers integrating with an

ion-exchange membrane, such as a proton exchange membrane. However, the connectivity of ion transport channels and local resistance for MEA are directly determined by the microphase-separated structure and hydration state of the membrane. These factors are critical for the proton conductivity of the membrane and the final cell output performance.[108] Frielinghaus et al.[109] studied the structure of Nafion@Pt model catalyst on a silicon substrate and its response to humidity by using GISANS and NR (Fig. 7). Microphase-separated structures were not observed within the Nafion film in GISANS measurements. In contrast, NR results revealed a 0.3 nm water layer sandwiched between the Nafion film and the Pt catalyst. The NR data also showed that the thickness of Nafion layer increased in high humidity. The phase-separated structure of the proton exchange membrane is important for fuel cell performance, because it provides the water channels for proton transport. GISANS has not yet resolved this structure in a confined membrane film. Further GISANS studies are needed for the triple-phase boundary, where the ionomer, the catalyst, and the reactant gas meet.

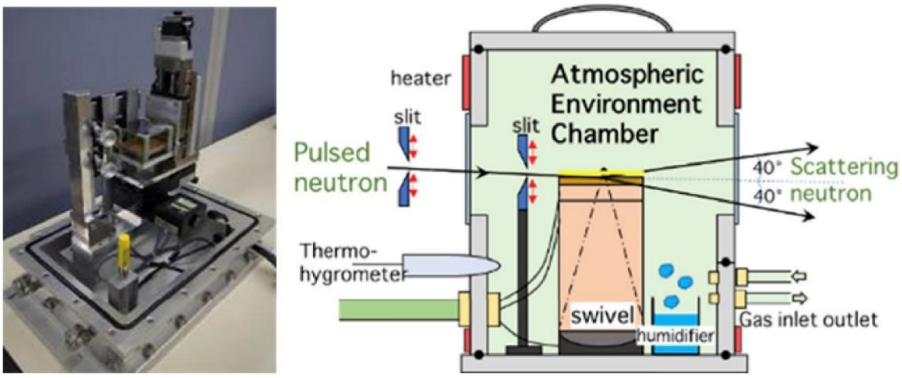


Fig. 7. Sample environment for GISANS investigation of the structure of a Nafion@Pt model catalyst and its humidity response.[109] Reprinted from Fig. 1 of Ref. 109, Copyright 2018, with permission from Elsevier.

5. Summary and Outlook

Grazing-incidence small-angle neutron scattering (GISANS) offers several distinct technical advantages. It has unique selectivity for surfaces and interfaces, high sensitivity to light elements, and allows precise contrast tuning via isotopic substitution. Furthermore, GISANS can also resolve both in-plane periodic structures and out-of-plane density distributions simultaneously. Thus, GISANS is widely applied for studying the interfacial nanostructures in soft matter, magnetic materials, energy materials and other fields. Importantly, GISANS can provides critical characterization data, which is valuable for establishing structure-property relationships and tracking dynamic evolution of materials during preparation and service. Although the scope of GISANS applications has grown markedly, the full potential of the technique has yet to be realized. This is particularly evident in the analysis of complex interfacial dynamics, which is hindered by the limited number of specialized GISANS instruments and the difficulty of data modeling based on the distorted wave Born approximation.[17] Thus, this powerful technique is expected to further broaden its application, with the emergence of user-friendly simulation frameworks and high-flux neutron sources.

Future advances in GISANS are expected to play a pivotal role in soft matter research. Biological membranes are composed of phospholipid bilayers, membrane proteins, and polysaccharides, which mediate critical biological processes such as material exchange and signal transduction. The interfacial architectures can be characterized non-destructively using GISANS, which reveals membrane structure, lateral fluidity, and responses to external stimuli such as drug molecules. Such insights are expected to advance our understanding of the molecular workings of membrane systems and accelerate the design of new therapeutic agents. Polarized GISANS enables to decouple nuclear and magnetic scattering, which gives access to in-plane magnetic correlations in thin films and multilayers over length scales ranging from a few nanometres to several hundred nanometres. This capability complements the depth profiling provided by neutron reflectometry. Although GISANS exhibits outstanding value for probing buried interfaces and magnetic domain structures, its application has been constrained by limited neutron flux. As a result, polarized GISANS measurements often require prohibitively long acquisition times on reactor sources, precluding the tracking of field-induced topological phase transitions. With the advent of high-brilliance neutron sources, substantial enhancements in both in-plane resolution and flux are anticipated. This progress is expected to enable the *in situ* detection of magnetic domain rearrangement and the evolution of chiral magnetic structures.[94]

In the realm of energy materials, GISANS is expected to establish comprehensive structure–property relationships of microstructure and device performance in organic solar cells. These advancements are expected to progressively improve power conversion efficiencies and operational lifetimes, thus supporting the industrial implementation of organic photovoltaics. Electrochemical energy devices, including batteries and fuel cells, can be used to store the renewable energy, such as wind and solar. As a result, electrochemical energy devices have seen rapid development and widespread research interest in recent years. The interfaces between electrode and electrolyte plays a critical role to the performance of electrochemical energy devices. However, the structural evolution of electrode–electrolyte interfaces during operation remains poorly understood. Against this background, GISANS stands out among characterization techniques. It serves as a powerful tool to probe buried interfaces in situ, showing great potential for electrochemical research. The passivation layer formed at the electrode–electrolyte interface is one of the most well-known interfacial problems in lithium-ion batteries. For example, the cycle life and safety are governed by the solid electrolyte interphase (SEI) formed at the anode.[110] In high-voltage lithium-ion batteries, performance strongly depends on the stability of the cathode electrolyte interphase (CEI).[111] These interfacial layers are nanoscale solid films formed at the electrode-electrolyte interface. They undergo mechanical fracture and electrochemical reconstruction during the charge and discharge cycling. Neutron reflectometry (NR) has been applied to investigate the electrode-electrolyte interface, which enables to map out one-dimensional scattering length density (SLD) profiles normal to the electrode-electrolyte interface.[112] This has greatly improved our understanding of SEI thickness and average chemical composition. However, NR

cannot capture lateral heterogeneity within the interface, which is a key factor determining ion transport pathways and interfacial stability. GISANS is expected to fill this gap. With the operation of next-generation high-brilliance spallation neutron sources such as the ESS and CSNS, and the development of dedicated grazing-incidence instruments, future studies should aim to improve the time resolution of GISANS to the next level. For example, the VSANS spectrometer at CSNS is now capable of simultaneously performing GISANS and GI-VSANS measurements.[36] In the near future, GISANS will enable to monitor the dynamic behavior of the SEI, including nucleation, growth, and repair processes. Specifically, GISANS resolves the lateral phase separation of organic and inorganic interfacial phases by combining in situ electrochemical cells with contrast matching, in which deuterated electrolytes selectively suppress bulk signals. This will provide nanoscale structural insights for designing next-generation electrode-electrolyte interfaces with high stability and fast ion transport.

Acknowledgment

The authors thank the CSNS institute. We acknowledge the Very Small Angle Neutron Scattering instrument at CSNS (https://cstr.cn/31113.02.CSNS.VSANS). This work was supported by the Xie Jia-Lin Project supported by the Institute of High Energy Physics of Chinese Academy of Sciences, and the Very Small Angle Neutron Scattering Instrument Project, supported by the Department of Science and Technology of Guangdong Province.

References

[1] Fan Y, Huang X, Ji J, Zhang W, Zhang J and Hou X 2024 *Angew. Chem. Int. Ed.* **63** e202403919
[2] Zhou X, Shen Q, Wang Y, Dai Y, Chen Y and Wu K 2024 *Natl. Sci. Rev.* **11** nwae272
[3] Zhu H, Liu Y, Mao L, Shen J, Zhu Z and Tang W 2010 *J. Semicond.* **31** 082003
[4] Li X, Dai L, Yang L, Chen X, Li N, Wang W, Chen H-S, Song W-L and Jiao S 2025 *Adv. Funct. Mater.* **35** 2414550
[5] Chen Z, Jiang Y, Shao Y-T, Holtz M E, Odstrčil M, Guizar-Sicairos M, Hanke I, Ganschow S, Schlom D G and Muller D A 2021 *Science* **372** 826
[6] Severin N, Dzhanoev A R, Lin H, Rauf A, Kirstein S, Palma C A, Sokolov I M and Rabe J P 2022 *Phys. Rev. Res.* **4** 023149
[7] Shard A G and Baker M A 2024 *J. Vac. Sci. Technol., A* **42** 050801
[8] Hosseini M, Arif M, Keshavarz A and Iglauer S 2021 *Earth-Sci. Rev.* **221** 103755
[9] Castellanos M M, McAuley A and Curtis J E 2017 *Comput. Struct. Biotechnol. J.* **15** 117
[10] Torikai N, Yamada N L, Noro A, Harada M, Kawaguchi D, Takano A and Matsushita Y 2007 *Polym. J.* **39** 1238
[11] Griggs W, Bull C, Barton C W, Griffiths R A, Caruana A J, Kinane C J, Nutter P W and Thomson T 2022 *Phys. Rev. Mater.* **6** 024403
[12] Karlsson M, Johansson L-G, Mazzei L, Froitzheim J and Wolff M 2024 *ACS*

Mater. Au **4** 346
[13] Rizell J, Zubayer A, Sadd M, Lundin F, Mozhzhukhina N, Eriksson F, Birch J, Vorobiev A, Xiong S and Matic A 2023 *Small Struct* **4** 2300119
[14] Hafner A, Gutfreund P, Toperverg B P, Geoghegan M and Sferrazza M 2021 *J. Phys.: Condens. Matter* **33** 364002
[15] Ogawa H, Kanaya T, Nishida K, Matsuba G, Majewski J P and Watkins E 2009 *J. Chem. Phys.* **131** 104907
[16] van de Kruijs R W E, Ul'yanov V A, Rekveldt M T, Fredrikze H, Pleshanov N K, Pusenkov V M, Syromyatnikov V G, Schebetov A F and Langridge S 2001 *Phys. B: Condens. Matter* **297** 180
[17] Köhler S, Arnold T, Birch J, Cárdenas M, Dorri S, Månsson M, Nylander T, Rogers S, Roth S V, Sassa Y and Wolff M 2026 *Adv. Colloid Interface Sci.* **349** 103757
[18] Garland M A, Mirzadeh S, Alexander C W, Hirtz G J, Hobbs R W, Pertmer G A and Knapp F F 2003 *Appl. Radiat. Isot.* **59** 63
[19] Jaksch S, Gutberlet T and Müller-Buschbaum P 2019 *Curr. Opin. Colloid Interface Sci.* **42** 73
[20] Passell L, Dickinson W C and Bartolini W 1961 *Rev. Sci. Instrum.* **32** 870
[21] Vineyard G H 1982 *Phys. Rev. B* **26** 4146
[22] Leroy F, Lazzari R and Renaud G 2007 *Surf. Sci.* **601** 1915
[23] Pedersen J S 1997 Adv. *Colloid Interface Sci.* **70** 171
[24] Xiao S Y, Wang S L, Wu B and Iwashita T 2026 *Chin. Phys. B* **35** 036106
[25] Nouhi S, Hellsing M S, Kapaklis V and Rennie A R 2017 *J. Appl. Crystallogr.* **50** 1066
[26] Wolff M, Pranzas K, Magerl A and Zabel H 2007 *Superlattices Microstruct.* **41** 190
[27] Lazzari R 2002 *J. Appl. Crystallogr.* **35** 406
[28] Babonneau D 2010 *J. Appl. Crystallogr.* **43** 929
[29] Pospelov G, Van Herck W, Burle J, Carmona Loaiza J M, Durniak C, Fisher J M, Ganeva M, Yurov D and Wuttke J 2020 *J. Appl. Crystallogr.* **53** 262
[30] Xie F, Xie M, Song B Y, Guo Q Y and Jiao X C 2024 *Chin. Phys. B* **33** 120101
[31] Müller-Buschbaum P 2013 *Polym. J.* **45** 34
[32] Chen J, Huang L, Yang T, Yang C, Zhong S, Sun G, Yan G and Liu D 2023 *Nucl. Instrum. Methods Phys. Res. A* **1051** 168228
[33] Widmann T, Kreuzer L P, Kühnhammer M, Schmid A J, Wiehemeier L, Jaksch S, Frielinghaus H, Löhmann O, Schneider H, Hiess A, Klitzing R v, Hellweg T and Müller-Buschbaum P 2021 *Appl. Sci.* **11** 4036
[34] Vorobiev A, Paracini N, Cárdenas M and Wolff M 2021 *Sci. Rep.* **11** 17786
[35] Mehler F, Jaksch S, Cárdenas M, Nickel B and Wolff M 2025 *Sci. Rep.* **15** 41184
[36] Chen Q, Zuo T, Ma C, He Y, Lin X, He Z, Han Z, Müller-Buschbaum P and Cheng H 2026 *J. Appl. Crystallogr.* **59** 1517
[37] Cai G, Li Y, Fu Y, Yang H, Mei L, Nie Z, Li T, Liu H, Ke Y, Wang X-L, Brédas J-L, Tang M-C, Chen X, Zhan X and Lu X 2024 *Nat. Commun.* **15** 2784
[38] Mattauch S, Koutsioubas A, Rücker U, et al. 2018 *J. Appl. Crystallogr.* **51** 646

[39] Feoktystov A V, Frielinghaus H, Di Z, Jaksch S, Pipich V, Appavou M-S, Babcock E, Hanslik R, Engels R, Kemmerling G, Kleines H, Ioffe A, Richter D and Bruckel T 2015 *J. Appl. Crystallogr.* **48** 61
[40] Heinz Maier-Leibnitz Zentrum 2014 *MLZ Newsletter 21*
[41] Heller W T, Urban V S, Lynn G W, Weiss K L, O'Neill H M, Pingali S V, Qian S, Littrell K C, Melnichenko Y B, Buchanan M V, Selby D L, Wignall G D, Butler P D and Myles D A 2014 *J. Appl. Crystallogr.* **47** 1238
[42] Do C, Nagy G and Heller W 2026 Extended Q-Range Small-Angle Neutron Scattering Diffractometer *Oak Ridge National Laboratory*
[43] Heiz Maier-Leibnitz Zentrum, Helmholtz-Zentrum Geesthacht 2015 *J. Large-Scale Res. Facil.* **1** A9
[44] Stellhorn A, Palma J G C, Backs A, Bergman A, Klautau A B, Kentzinger E, Bednarski-Meinke C, Tober S, Blackburn E, Barthel J, Steinke N-J, Petrilli H M and Miranda I P 2026 *arXiv:2604.02824v1*
[45] Wolff M, Herbel J, Adlmann F, Dennison A J C, Liesche G, Gutfreund P and Rogers S 2014 *J. Appl. Crystallogr.* **47** 130
[46] Glavic A and Stahn J 2018 *Rev. Sci. Instrum.* **89**
[47] Arnold T, Birch J, Cárdenas M, Jena S K, Köhler S, Månsson M, Nylander T, Rennie A, Rogers S, Roth S and Wolff M 2025 SAGA - A Swedish initiative for a GISANS instrument at ESS *SAGA Project Team*
[48] Jaksch S, Lieutenant K, Babcock E and Frielinghaus H 2023 *Nucl. Instrum. Methods Phys. Res. A* **1048** 167919
[49] De Campo L, Gilbert E, Knott R, Mata J, Sokolova A, Whitten A, Wood K and Wu C-M 2021 *ANSTO User Meeting 2021*
[50] Yamazaki D, Maruyama R, Aoki H, Hanashima T, Akutsu-Suyama K, Miyata N and Soyama K 2025 *Quantum Beam Sci.* **9** 20
[51] Chen Q, Künniger T, Song Q, Zhang K, Chumakov A, Bulut Y, Harder C, Müller-Buschbaum P, Roth S V and Braun A 2024 *Adv. Funct. Mater.* **34** 2402924
[52] Vagias A, Manouras T, Gutfreund P, Le Dû M P, Koufakis E, Kosbahn D P, Baier T, Buchner A, Wolf M, Chiappisi L, Dahint R, Vamvakaki M and Müller-Buschbaum P 2026 *Polymer* **357** 130029
[53] Urwick A N, Bastianini F, Pérez G E and Dunbar A 2022 *Energy Rep.* **8** 23
[54] Newby G E, Watkins E B, Merino D H, Staniec P A and Bikondoa O 2015 *RSC Adv.* **5** 104164
[55] Metwalli E, Moulin J-F, Gebhardt R, Cubitt R, Tolkach A, Kulozik U and Müller-Buschbaum P 2008 *Langmuir* **25** 4124
[56] Schlipf J, Bießmann L, Oesinghaus L, Berger E, Metwalli E, Lercher J A, Porcar L and Müller-Buschbaum P 2018 *J. Phys. Chem. Lett.* **9** 2015
[57] Debas M, Mégroz E, Moir M, Darwish T, Glavic A and Salentinig S 2026 *ChemRxiv*
[58] Kreuzer M, Kaltofen T, Steitz R, Zehnder B H and Dahint R 2011 *Rev. Sci. Instrum.* **82**
[59] Vagias A, Manouras T, Buchner A, Gutfreund P, Porcar L, Jacques M, Chiappisi

L, Kosbahn D P, Wolf M, Guasco L, Dahint R, Vamvakaki M and Müller-Buschbaum P 2024 *J. Appl. Crystallogr.* **57** 1978
[60] Kentzinger E, Frielinghaus H, Rücker U, Ioffe A, Richter D and Brückel T 2007 *Phys. B: Condens. Matter* **397** 43
[61] Honecker D, Dresen D and Disch S 2015 Dipolar coupling in arrays of magnetic nanoparticles, studied using time-of-flight polarized GISANS *Institut Laue-Langevin*
[62] Sharaku 2026 Sample Environment (SE) at BL17 *J-PARC*
[63] ANSTO 2026 Sample Environment: Quokka
[64] Walz M, Magerl A, Wolff M and Zabel H 2007 *Superlattices Microstruct.* **41** 185
[65] Hamley I W, Burholt S, Hutchinson J, Castelletto V, da Silva E R, Alves W, Gutfreund P, Porcar L, Dattani R, Hermida-Merino D, Newby G, Reza M, Ruokolainen J and Stasiak J 2016 *Biomacromolecules* **18** 141
[66] Zec N, Mangiapia G, Zheludkevich M L, Busch S and Moulin J-F 2020 *Phys. Chem. Chem. Phys* **22** 12104
[67] Kim K H, Huh Y, Song I, Ryu D Y, Son J G and Bang J 2024 *J. Polym. Sci.* **62** 679
[68] Leibler L 1980 *Macromolecules* **13** 1602
[69] Bates F S and Fredrickson G H 1999 *Phys. Today* **52** 32
[70] Gu Y and Wiesner U 2015 *Macromolecules* **48** 6153
[71] Müller-Buschbaum P, Gutmann J S, Cubitt R and Petry W 2004 *Phys. B: Condens. Matter* **350** 207
[72] Wolff N, Gerth S, Gutfreund P and Wolff M 2014 *Soft Matter* **10** 8420
[73] Hu M, Li X, Heller W T, Bras W, Rzayev J and Russell T P 2023 *Macromolecules* **56** 2418
[74] Gan X, Chen Z, Steinmetz C, Hu M, Fink Z, Wu X, Heller W T, Coughlin E B and Russell T P 2025 *Macromolecules* **58** 3832
[75] Vargas-Ruiz S, Soltwedel O, Micciulla S, Sreij R, Feoktystov A, von Klitzing R, Hellweg T and Wellert S 2016 *Langmuir* **32** 11928
[76] Paracini N, Gutfreund P, Welbourn R, Gonzalez-Martinez J F, Zhu K, Miao Y, Yepuri N, Darwish T A, Garvey C, Waldie S, Larsson J, Wolff M and Cárdenas M 2023 *ACS Appl. Mater. Interfaces* **15** 3772
[77] Bosworth J K, Dobisz E A, Hellwig O and Ruiz R 2011 *Macromolecules* **44** 9196
[78] Madathil K, Hekmatnia B, Ardebili H and Stein G E 2023 *Polymer* **288** 126469
[79] Kambe Y, Arges C G, Czaplewski D A, Dolejsi M, Krishnan S, Stoykovich M P, de Pablo J J and Nealey P F 2019 *Nano Lett.* **19** 4684
[80] Alexander H and Müller-Buschbaum P 2015 *IUCrJ* **2** 106
[81] Müller-Buschbaum P, Kaune G, Haese-Seiller M and Moulin J-F 2014 *J. Appl. Crystallogr.* **47** 1228
[82] Barbey R, Lavanant L, Paripovic D, Schüwer N, Sugnaux C, Tugulu S and Klok H-A 2009 *Chem. Rev.* **109** 5437
[83] Zoppe J O, Ataman N C, Mocny P, Wang J, Moraes J and Klok H-A 2017 *Chem. Rev.* **117** 1105

[84] Liu Y, Liu Y, Wu Y and Zhou F 2025 *ACS Nano* **19** 11576
[85] Zhao K, Li M, Geng H, Gao Z, Zhang X, Sekhar K P C, Zhang P and Cui J 2024 *Biomacromolecules* **25** 6727
[86] Yang W J, Neoh K-G, Kang E-T, Teo S L-M and Rittschof D 2014 *Prog. Polym. Sci.* **39** 1017
[87] Li M and Pester C W 2020 *Polymers* **12** 1553
[88] Berret J-F 1997 *Langmuir* **13** 2227
[89] Steitz R, Müller-Buschbaum P, Schemmel S, Cubitt R and Findenegg G H 2004 *Europhys. Lett.* **67** 962
[90] Sudhahar C G, Haney R M, Xue Y and Stahelin R V 2008 *Curr. Drug Targets* **9** 603
[91] Jaksch S, Holderer O, Frielinghaus H, Koutsioubas A, Zolnierczuk P, Hayward D W, Förster S and Müller-Buschbaum P 2021 *Front. Phys.* **9** 628219
[92] Jiles D C 2003 *Acta Mater.* **51** 5907
[93] Li S, Wang X and Rasing T 2023 *Interdiscip. Mater.* **2** 260
[94] Zhang H, Zhang Y, Hou Z, Qin M, Gao X and Liu J 2023 *Mater. Futures* **2** 032201
[95] Liyanage W L N C, Tang N, Quigley L, Borchers J A, Grutter A J, Maranville B B, Sinha S K, Reyren N, Montoya S A, Fullerton E E, DeBeer-Schmitt L and Gilbert D A 2023 *Phys. Rev. B* **107** 184412
[96] Wiedemann B, Chacon A, Zhang S L, Khaydukov Y, Hesjedal T, Soltwedel O, Keller T, Mühlbauer S, Adams T, Halder M, Pfleiderer C and Böni P 2017 *arXiv:1710.00544v1* 1710.00544
[97] Hu W, Zhang Z, Liao Y, Li Q, Shi Y, Zhang H, Zhang X, Niu C, Wu Y, Yu W, Zhou X, Guo H, Wang W, Xiao J, Yin L, Liu Q and Shen J 2023 *Nat. Commun.* **14** 2562
[98] Skjærvø S H, Marrows C H, Stamps R L and Heyderman L J 2020 *Nat. Rev. Phys.* **2** 13
[99] Pip P, Glavic A, Skjærvø S H, Weber A, Smerald A, Zhernenkov K, Leo N, Mila F, Philippe L and Heyderman L J 2021 *Nanoscale Horiz.* **6** 474
[100] Ragupathy P, Bhat S D and Kalaiselvi N 2023 *Wiley Interdiscip. Rev. Energy Environ.* **12** e464
[101] Yeh N and Yeh P 2013 *Renew. Sustain. Energy Rev.* **21** 421
[102] Krauss F T, Pantenburg I and Roling B 2022 *Adv. Mater. Interfaces* **9** 2101891
[103] Pan Q, Guo D, Gao X, Heere M, Lu W, Vietor T and Gao Y 2024 *Int. J. Hydrogen Energy* **87** 409
[104] Zhang Y, He Z, Liu X, Zhang Y, Song C, Yang X, Xin J and Liu J 2025 *Chem. Eng. J.* **525** 170094
[105] Liu H, Li Y, Nie Z, et al. 2025 *ACS Appl. Mater. Interfaces* **17** 66924
[106] Liu X, Zeng Y, Yuan W, Zhang G, Zheng H and Chen Z 2024 *Energy Rev.* **3** 100066
[107] Paul N, Brumbarov J, Paul A, Chen Y, Moulin J-F, Müller-Buschbaum P, Kunze-Liebhauser J and Gilles R 2015 *J. Appl. Crystallogr.* **48** 444
[108] Bhosale A C, Ghosh P C and Assaud L 2020 *Renew. Sustain. Energy Rev.* **133**

110286
[109] Ueda S, Koizumi S, Ohira A, Kuroda S and Frielinghaus H 2018 *Phys. B: Condens. Matter* **551** 309
[110] Mohd Harun M H Z and Azam M A 2026 *J. Energy Storage* **162** 122133
[111] Feng L, Yang H, Wang Y, Wen B, Zheng Y and Li B 2026 *Energy Storage Mater.* **88** 105100
[112] Wu K, Zhan X, Ran P, Wang F, Zhu T, Zhao J and Zhao E 2026 *ACS Nano* **20** 3855